Mon. Not. R. Astron. Soc. **299,** 965–976 (1998)

L 43: the late stages of a molecular outflow

S. J. Bence,[1]★ R. Padman,[1] K. G. Isaak,[2]† M. C. Wiedner[1] and G. S. Wright[3]

[1]*Mullard Radio Astronomy Observatory, Cavendish Laboratory, Madingley Road, Cambridge CB3 0HE*
[2]*Five Colleges Radio Astronomy Observatory, University of Massachussetts, Amherst, MA 01003, USA*
[3]*Joint Astronomy Centre, 660 N. A'ohōkū Place, University Park, Hilo, Hawaii 96720, USA*

Accepted 1998 May 1. Received 1998 May 1; in original form 1997 February 28

ABSTRACT

Our new 21-arcsec resolution CO $J = 2 \rightarrow 1$ map of the L 43 dark cloud shows a poorly collimated molecular outflow, with little evidence for wings at velocities $\gtrsim$10 km s^{-1}. The outflow appears not to be currently driven by a jet: its structure can instead be modelled as a slowly expanding shell. The shell may be compressed either by a wide-angled wind catching up with an existing shell (as in the case of planetary nebulæ), or by the thermal pressure of a hot low-emissivity medium interior to the shell. The outflow is most probably in a late stage of evolution, and appears to be in the process of blowing away its molecular cloud. We also present a 45-arcsec resolution CO $J = 1 \rightarrow 0$ map of the whole molecular cloud, showing that the outflow structure is clearly visible even in the integrated intensity of this low excitation line, and suggesting that rapid mapping may prove useful as a way of finding regions of outflow activity. We also examine the immediate surroundings of the driving source with 450 μm imaging: this confirms that the outflow has already evacuated a bay in the vicinity of the young stellar object.

Key words: stars: formation – stars: mass-loss – ISM: individual: L43 – ISM: jets and outflows – ISM: kinematics and dynamics.

1 INTRODUCTION

Over 250 molecular outflows are now known (Fukui et al. 1993; Wu, Huang & He 1996), but only a small fraction have yet been mapped at high angular resolution. Authors who *have* chosen to observe at high spatial resolution have tended to concentrate on bright, collimated flows, and usually those which show high velocity line wings [e.g. NGC 2024 (Richer, Hills & Padman 1992); RNO 43 (Bence, Richer & Padman 1996), NGC 2264G (Lada & Fich 1996); VLA 1623 (Dent, Matthews & Walther 1995)]. A model in which ambient cloud material is swept-up by the passage of a supersonic jet can account for the main features of these collimated outflows (e.g. Bence et al. 1996). Although difficulties remain (Lada & Fich 1996), some consensus has been reached that jets drive directly many molecular outflows.

Although the simplicity of the jet-driven outflow model is appealing, some outflows do not, at least at a first glance, admit such a simple explanation. For example, the archetypical L 1551 molecular outflow (Snell, Loren & Plambeck 1980) is not well collimated, nor is the outflow in the L 43 dark cloud. Although a number of authors have mapped its bright central region (see Section 2), the L 43 outflow has not previously been mapped over its total extent. We thus decided to map the whole outflow, in the CO $J = 2 \rightarrow 1$ line, at high resolution (21 arcsec), with the aim of determining the mechanism responsible for driving the outflow, and of comparing the structure with that observed in L 1551. We also mapped the L 43 dark cloud at lower (45 arcsec) resolution, in the CO $J = 1 \rightarrow 0$ line, so that we could determine the structure of the whole cloud in a reasonable amount of observing time.

2 PREVIOUS OBSERVATIONS

The L 43 outflow is located in the northern part of the Ophiuchus complex at a distance of 160 pc (Herbst & Warner 1981). The POSS plates show extinction over an area $\sim 1.7 \times 0.3$ pc^2, at PA +68° (see, e.g., Parker, Padman & Scott 1991), although it appears that CO extends roughly twice as far as the extinction in all directions (Elmegreen & Elmegreen 1979). The cloud contains two reflection nebulosities, RNO 90 and RNO 91 (Cohen 1980), each illuminated by a young stellar object. The CO outflow is associated with RNO 91, which is also identified as IRAS 16316-1540.

IRAS 16316-1540 is visible at 12, 25, 60 and 100 μm, and Myers et al. (1988) report a refined position of $\alpha = 16^{\rm h}31^{\rm m}38^{\rm s}.0$, $\delta = -15°40'50''$ (uncertain to ~2 arcsec) and this is the position we shall use in this paper. André & Montmerle (1994) classify it as a Class II protostar, i.e. an embedded T Tauri star and it seems, therefore, that the central object is in a transition phase between a protostar and a main-sequence star. The bolometric luminosity is

★ E-mail: S.J.Bence@mrao.cam.ac.uk
† Present address: Department of Astronomy, University of Maryland, College Park MD 20742, USA.

4.3 $L_\odot$ (Terebey, Chandler & André 1993) and the mass 0.5 $M_\odot$ (Levreault 1988). RNO 91 is thus a low-mass, low-luminosity YSO, yet still much more luminous than a zero-age main-sequence star of the same mass.

The CO outflow in L 43 has previously been studied by Levreault (1988), Myers et al. (1988), Mathieu et al. (1988) and Parker et al. (1988). Of these, only Mathieu et al. and Parker et al. publish CO maps: these show an outflow elongated approximately north–south with a blue-shifted lobe to the south and a red-shifted lobe to the north. The lobes are spatially separated, i.e. there is very little overlapping red- and blueshifted emission, and this suggests that the outflow has a moderate angle of inclination to the plane of the sky. The maps extend north–south only slightly beyond the extinction visible on the POSS plate. The observations presented in this paper show that this represents only a small fraction of the outflow. All authors report very narrow lines ($\sim$ 1.8 km s^{-1}) centred on $V_{\rm LSR} = 0.2$ km s^{-1}(see Section 4.1 for a discussion of the true value of the systemic $V_{\rm LSR}$).

Mathieu et al. (1988) also present an *I*-band CCD image of the L 43 cloud. This shows that RNO 91 lies inside a parabolic-shaped region, which has lower extinction than its surroundings. They refer to this as a 'bay' which opens towards the south, with RNO 91 lying near the closed end to the north. The bay has a higher surface luminosity than the surroundings and has a reflection nebulosity along its borders. Overlays of the CO outflow on the CCD image show that the blue lobe is coincident in projection with the bay. Mathieu et al. conclude that the outflow has blown through the dense core into a lower density medium, in the process exposing both the driving YSO and an outflow cavity.

The CCD image of Mathieu et al. (1988) shows a 7 arcsec spur to the south. This is also seen by Schild, Weir & Mathieu (1989) and Scarrott, Draper & Tadhunter (1993). Observations of the polarisation by Scarrott et al. suggest that the 'bay' and the optical extension lie close to the plane of the sky, unlike the CO axis, which to the south is inclined towards us at a moderate angle.

3 OBSERVATIONS

Our observations of ^{12}CO $J = 2 \rightarrow 1$ were obtained in 1995 February using the 15-m James Clerk Maxwell Telescope (JCMT) on Mauna Kea, Hawaii. The beam size at 230 GHz is about 21 arcsec. All the data were taken with the digital autocorrelation spectrometer (DAS) and using continuous raster scanning such that the telescope moves continuously over a long (> 50 arcsec) row. The spectrometer integrates, boxcar fashion, for the time it takes the telescope to move 5 arcsec, and the results are double-buffered, so that the integration is continuous over the row. An OFF spectrum is taken at the start and end of each row, and a linearly interpolated OFF spectrum is then subtracted from each ON spectrum. Approximately 6400 spectra were obtained which have been reduced using the spectral line reduction package SPECX. Most of the map is Nyquist sampled, but to the far north the map is beam sampled owing to time constraints.

Lower resolution ^{12}CO $J = 1 \rightarrow 0$ data were obtained with the 15-element QUARRY array receiver on the FCRAO 14-m telescope. The beam size at 115 GHz is about 45 arcsec. The observations were taken in 1996 May and June in position switching mode. Approximately 2200 spectra were obtained on a 25 arcsec grid and have been reduced using SPECX. Although the main region of outflow activity is Nyquist sampled, the rest of the map is undersampled since we again wished to cover as large a fraction of the cloud as possible.

The continuum map was obtained in 1992 August at the JCMT, using the single element bolometer, UKT 14. A filter with a nominal wavelength of 450μm was used, with a 65-mm aperture giving a resolution of 17.5 arcsec. The observations consist of a single 31 pixel $\times$19 pixel raster map with a pixel size of 5×5 arcsec^2 and with 4 seconds of integration time per pixel. We used a 40 arcsec chop throw in azimuth. Correction for the atmosphere was achieved by relating the observing opacity at 450 μm to the measured opacity at 225 GHz, using the conversion given by Stevens & Robson (1994). Calibration was achieved by making a map of Uranus, and comparing the expected peak flux, with the bolometer read-out. We find the noise on the map to be of 0.0074 Jy arcsec^{-2}, after the 4-s integration (this corresponds to a NEFD of 2.6 Jy beam^{-1} s$^{1/2}$). The map has been reconstructed using the dual-beam maximum entropy program DBMEM (Richer 1992).

4 RESULTS

4.1 The CO outflow: JCMT observations

The CO $J = 2 \rightarrow 1$ integrated intensity map of the L 43 dark cloud (Fig. 1) shows that the region of enhanced linewidth (hereinafter the 'disturbed' region; see Section 5.3 for a discussion of this terminology) extends over an area of about 400×1000 arcsec^2. At the assumed distance of 160 pc, this area corresponds to about 0.3×0.8 pc^2. The outflow is strongly asymmetric, the emission being much stronger and more extended to the SE than to the NW. To the SE the map shows a very sharp boundary between disturbed and undisturbed cloud, with the disturbed region forming a shell structure dominated by emission along its edges, and with relatively little integrated intensity in its interior. A jet-like feature, about 150 arcsec long, extends to the extreme SE, directed approximately away from RNO 91. To the NW, there is a faint ring of emission, dominated by a bright arc to the north of RNO 91.

Fig. 2 shows the red POSS plate of the L 43 cloud region with contours of the ^{12}CO $J = 2 \rightarrow 1$ emission overlaid. The obscuration runs across the plate at PA $\sim$70°. The outflow extends well beyond the optical extinction to the south, but not to the north. The major axis of the outflow is inclined at approximately PA $-35°$, i.e. almost perpendicular to the major axis of the cloud.

The bright extension to the north can be seen more clearly in the expanded integrated intensity map of the region about RNO 91, shown in Fig. 3. The northern extension has a counterpart to the south and consists of a bright ridge of hotspots along an axis inclined at PA +13°. Spectra at the position of RNO 91, and at two symmetrical positions along this axis, are shown in Fig. 4. The spectrum to the south is predominantly blueshifted with respect to the systemic $V_{\rm LSR}$. In addition to the central component, which is approximately at the systemic $V_{\rm LSR}$, a second component can clearly be seen, centred at about -3.5 km s^{-1}. Each component has a width of $\sim$2 km s^{-1}. The spectrum to the north is slightly brighter and it too shows evidence for two components, with the second component on the redshifted side. Here both the separation and the width of the two components is lower. The spectrum in the centre is the weakest, and shows only a single component. There is no evidence over the full spectral range for any very high-velocity features, either in these spectra, or elsewhere in the map. These spectra are representative of the velocity structure, in that the southern lobe is predominantly blueshifted, while the northern lobe is predominantly redshifted. Spatially separated red and blue lobes are indicative of an outflow at intermediate angles of inclination, θ, to the sky and Mathieu et al. (1988) suggest that for the

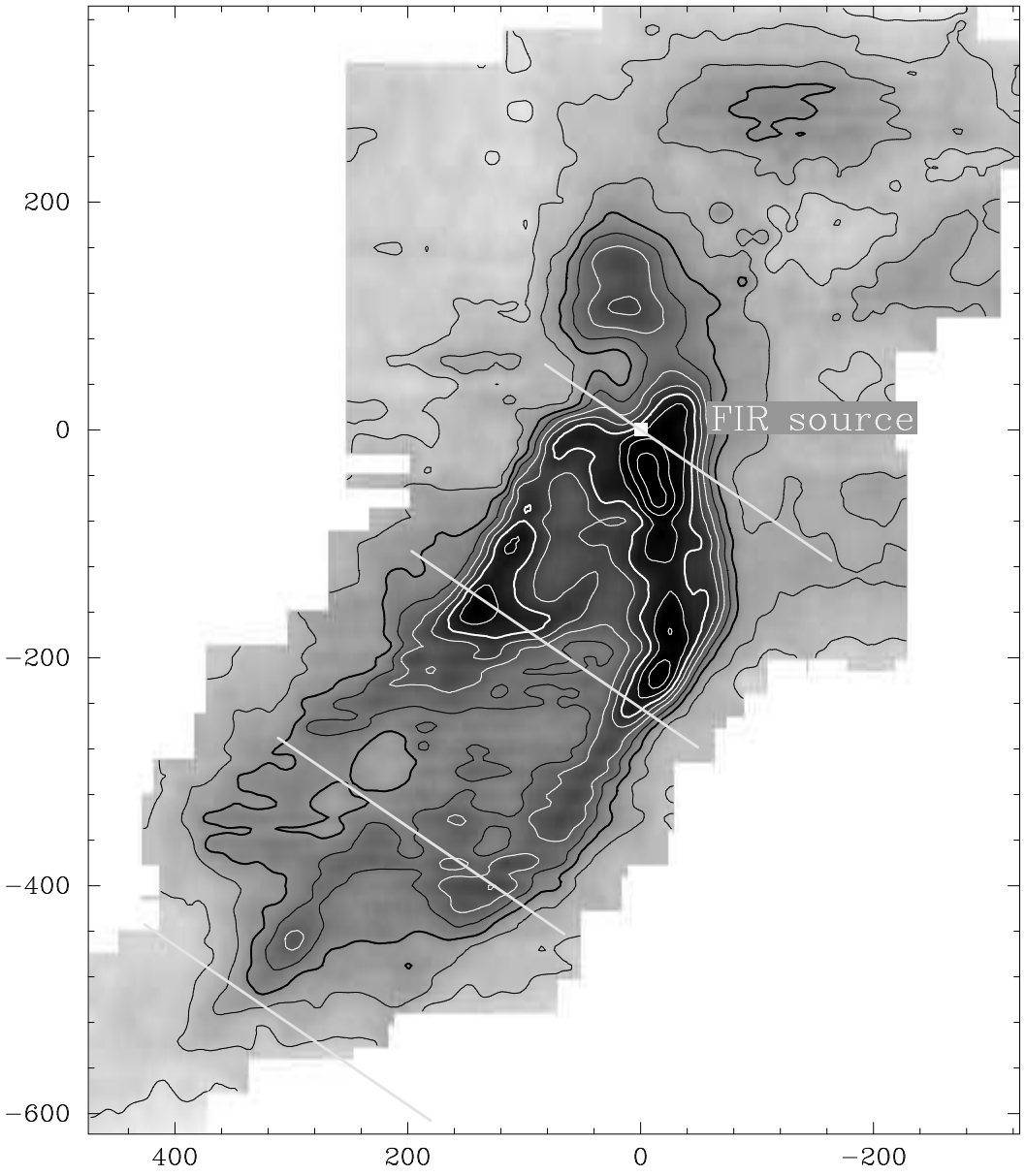

Figure 1. Image of the integrated intensity $\int_{-5}^{5} T_{\rm R}^{*} {\rm d}v$ of the ^{12}CO $J = 2 \rightarrow 1$ line in the L 43 dark cloud. Offsets are given in arcseconds from the YSO which is at $\alpha = 16^{\rm h}31^{\rm m}38^{\rm s}$, $\delta = -15°40'50''$. The map has been convolved to a resolution of ~25 arcsec. The 12 contours are at levels $4 + 3n$ K km s^{-1} for $n = 0, 1, \ldots, 11$. The four lines perpendicular to the flow axis, mark the extremes of the cuts used in Fig. 10.

outflow $\theta \approx 45°$. However, the strengths of the lines shown in the figure are atypical, and most of the emission to the north is much weaker than to the south.

Fig. 5 shows the average of all the spectra in the CO map. The peak of the line is at $V_{\rm LSR} = 0.3$ km s^{-1}, although the emission is dominated by outflowing material and the quiescent cloud has a velocity $V_{\rm LSR}$ of 0.7 km s^{-1}, as can be found by taking the peak of the average spectrum of the emission outside the obvious outflowing region.

4.2 The CO outflow: FCRAO observations

The ^{12}CO $J = 1 \rightarrow 0$ QUARRY image of the whole cloud can be seen in Fig. 6. Much of the cloud has been covered by our observations, and the map extends beyond the obvious extinction on the red POSS plate. There is no evidence for a second molecular outflow in the cloud, and in particular, there appears to be no outflow associated with RNO 90.

4.3 The continuum data

Our 450-μm map is shown in Fig. 7. The driving source is clearly visible, with the contours peaking at the position of the FIR source, and there is also a slight extension to the south, approximately aligned with the CO outflow axis. The total flux from the YSO at 450 μm is 92 Jy. Most of the rest of the emission lies approximately on the edges of the parabolic shell seen in the 2-μm infrared continuum image from Hodapp (1994) [also shown in Fig. 7]. The infrared image clearly shows the nebulosity RNO 91 extending over 20×25 arcsec^2, which at a distance of 160 pc corresponds to 3200×4000 au^2. That the emission is so extended strongly supports the suggestion that the emission is caused by light reflected in the cloud.

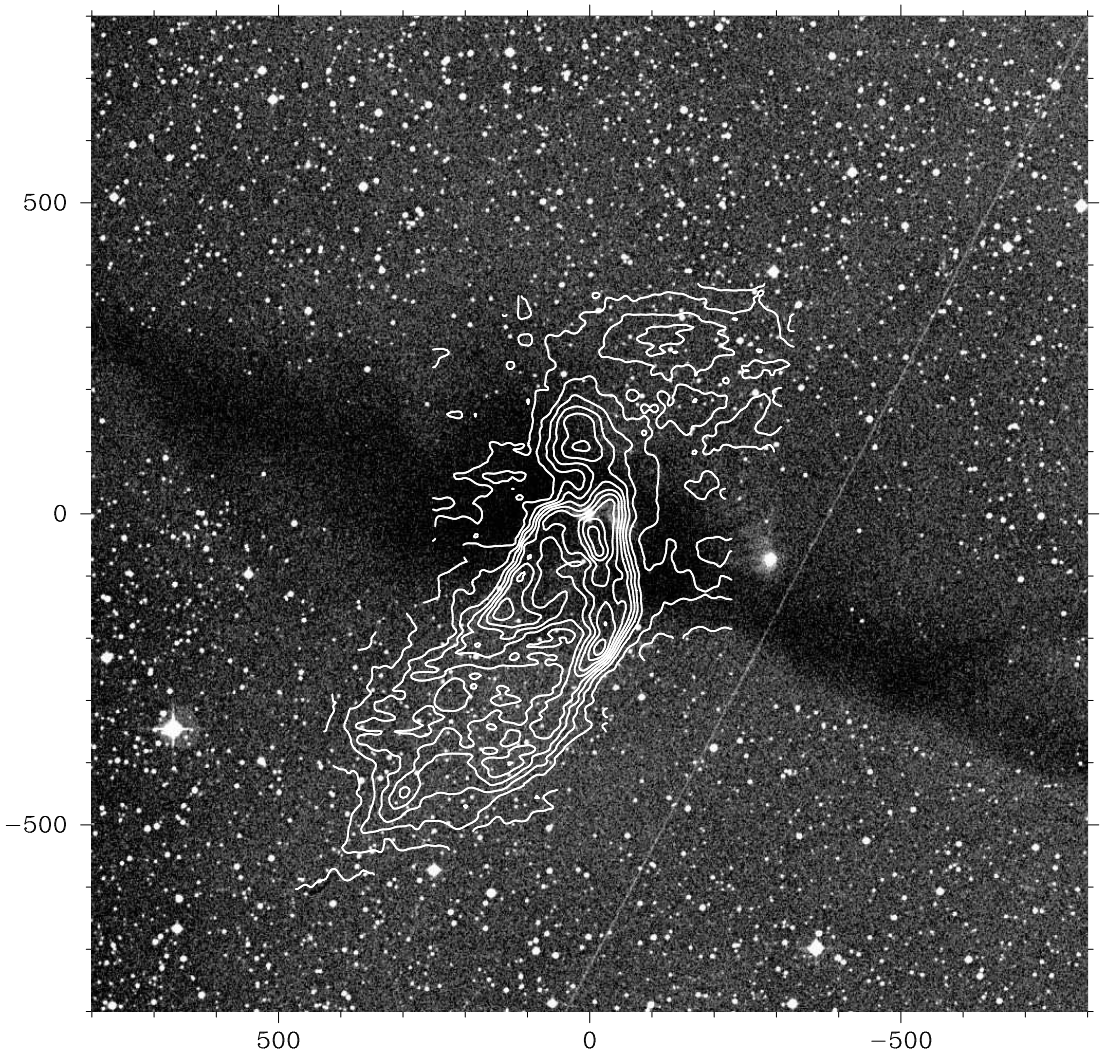

Figure 2. ^{12}CO $J = 2 \rightarrow 1$ contours overlaid on the red POSS plate of the L 43 region. Offsets are given in arcsec from the YSO, which is at $\alpha = 16^{h}31^{m}38^{s}$, $\delta = -15°40'50''$. Note that RNO 90 can be seen at about $-280''$, $-80''$. The contours are at the same levels as in Fig. 1.

The structure seen in the infrared continuum image of Hodapp (1994) is very similar to that observed by Mathieu et al. (1988) in the *I* band, and is presumably a result of scattering from the edge of a cavity which has been evacuated by the CO outflow. That the CO outflow axis and the axis of the reflection parabola are so well aligned, and that the extremities of the CO outflow align so well with the extremities of the bay, further strengthens this viewpoint. It is interesting to note that the position of RNO 91 is not at the apex of the parabola but rather offset ~50 arcsec from it, along its axis; this is most probably an inclination effect similar to that seen in L 1551 IRS 5 (Moriarty-Schieven & Snell 1988).

5 DISCUSSION

5.1 Asymmetry

It is apparent from our CO observations that the molecular outflow in L 43 is strongly asymmetric, with the blueshifted lobe to the south dominating the redshifted lobe to the north, both in extent and in brightness. This can be quantified by the ratio of blueshifted to redshifted emission in the average spectrum, i.e.

$$r = \frac{\int_{-5.3}^{0.7} T_{\rm R}^{*} \mathrm{d}v}{\int_{0.7}^{6.7} T_{\rm R}^{*} \mathrm{d}v} = 2, \qquad (1)$$

(where the integration limits have been chosen to be symmetric about the $V_{\rm LSR}$ of the quiescent cloud). It should be remembered, however, that mass is not a well-determined quantity, since an optically thick line core can hide a significant mass. The momentum analogue of equation (1) gives a ratio of 5.2; the energy equivalent gives 13.8. These high values reflect the broad wing on the blueshifted side of the line, but the momentum ratio in particular poses a problem, because we expect the momentum to be the same on both sides of the YSO. Apparent momentum imbalance is not uncommon, with a number of well-known molecular outflows, such as NGC 2024 (Richer et al. 1992) and HH 46–47 (Chernin & Masson 1991), showing similar asymmetries. In these cases the authors cite environmental effects as the cause of the lack of bipolarity, e.g. a lack of ambient material to sweep up.

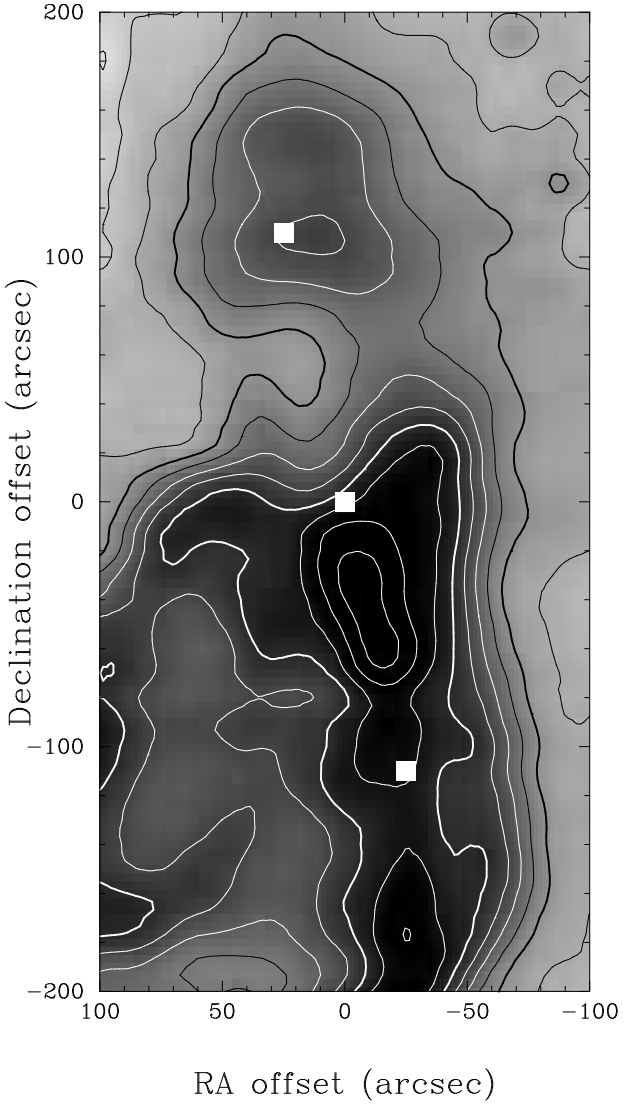

Figure 3. Image of the integrated intensity $\int_{-5}^{5} T_R^* \mathrm{d}v$ of the ^{12}CO $J = 2 \rightarrow 1$ line in the vicinity of RNO 91 in the L 43 dark cloud. Offsets are given in arcsec from the YSO. The map has been convolved to a resolution of ~25 arcsec. The 12 contours are at levels $4 + 3n$ K km s^{-1} for $n = 0, 1, \ldots, 11$. The white squares mark the positions of the spectra shown in Fig. 4.

The asymmetry in L 43 is also visible in the infrared continuum images, and again this is not unique to this source. Staude & Elsässer (1993) give a review of the optical and infrared structure of bipolar nebulae. NGC 2261, for example, shows an asymmetric structure at optical wavelengths, as does L 1551 IRS 5. Staude & Elsässer attribute any lack of symmetry to environmental effects similar to those described above. Another possibility is that this asymmetry results from inclination effects (Whitney & Hartmann 1993).

Lack of ambient material may be the cause of the asymmetry in L 43, but another possibility is that the CO to the north has become unobservable owing to dissociation by UV radiation. Fig. 6 shows that the northern edge of the ambient cloud has brighter CO $J = 1 \rightarrow 0$ emission than the southern edge (i.e. the integrated intensity contours appear to be offset to the north), possibly indicating a higher UV flux to the north.

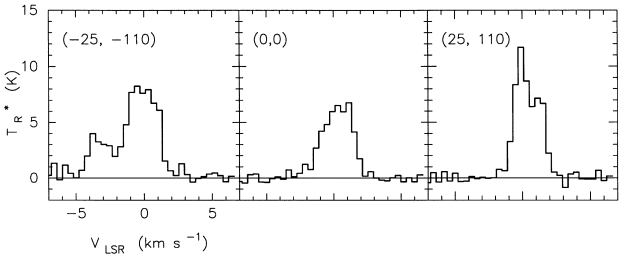

Figure 4. Three ^{12}CO $J = 2 \rightarrow 1$ spectra of L 43 showing emission in the line wings. The spectra are at the positions shown in Fig. 3, their offsets being given in arcsec from RNO 91.

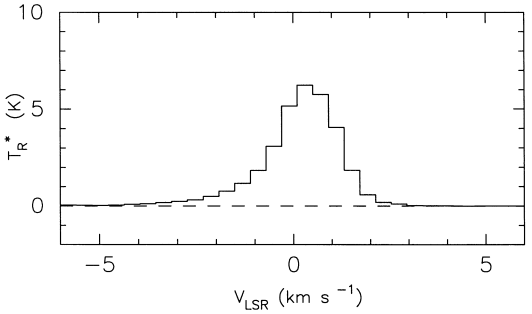

Figure 5. The average of all the spectra in the CO map.

5.2 The velocity structure

Fig. 8 shows velocity–channel maps of the L 43 outflow. These maps exhibit a number of long linear features. One of these, to the far SE of the outflow, is also visible in the integrated intensity map (Fig. 1), and it is approximately aligned with the YSO. These observations strongly suggest that a jet from the YSO has propagated to the end of the disturbed region. The velocity structure is not, however, that of a bowshock. This can be seen from the channel maps, which show no evidence for the highest velocities appearing furthest away from the YSO as would be expected for bowshock entrainment (Bence et al. 1996). Neither does the structure broaden nearer to the YSO, as would be expected of a bowshock. Furthermore, the velocities observed are very low (< 2 km s^{-1} from the systemic V_{LSR}) and, even in sources such as RNO 43 which lie close to the plane of the sky, this is abnormal. One possible explanation for these observations is that CO emission originates in a turbulent boundary layer, which is moving at a much lower velocity than the driving jet. The entrainment mechanism would then presumably be due to sideways ejection of jet material as a result of internal shocks [see Raga et al. (1993) for a detailed discussion of this mechanism].

Other linear features, however, clearly do *not* point towards the YSO. These are visible to the south of the YSO, particularly in the four channels between -2.75 and -1.25 km s^{-1}. In the vicinity of the YSO they delineate the edge of the reflection nebulosity seen in Fig. 7, and they remain linear further from the YSO. Further, the velocity of these features decreases with distance from the YSO. A full discussion of these observations is given in Section 5.5.3, and a kinematic model is presented in Section 6.

These channel maps also show the lack of overlapping blue- and redshifted emission. As has been discussed before, this is normally indicative of an outflow whose axis lies at an intermediate angle to the plane of the sky: biconical radial outflows in the plane of the sky show blue- and redshifted emission originating from their front and back faces, while outflows close to the line of sight show

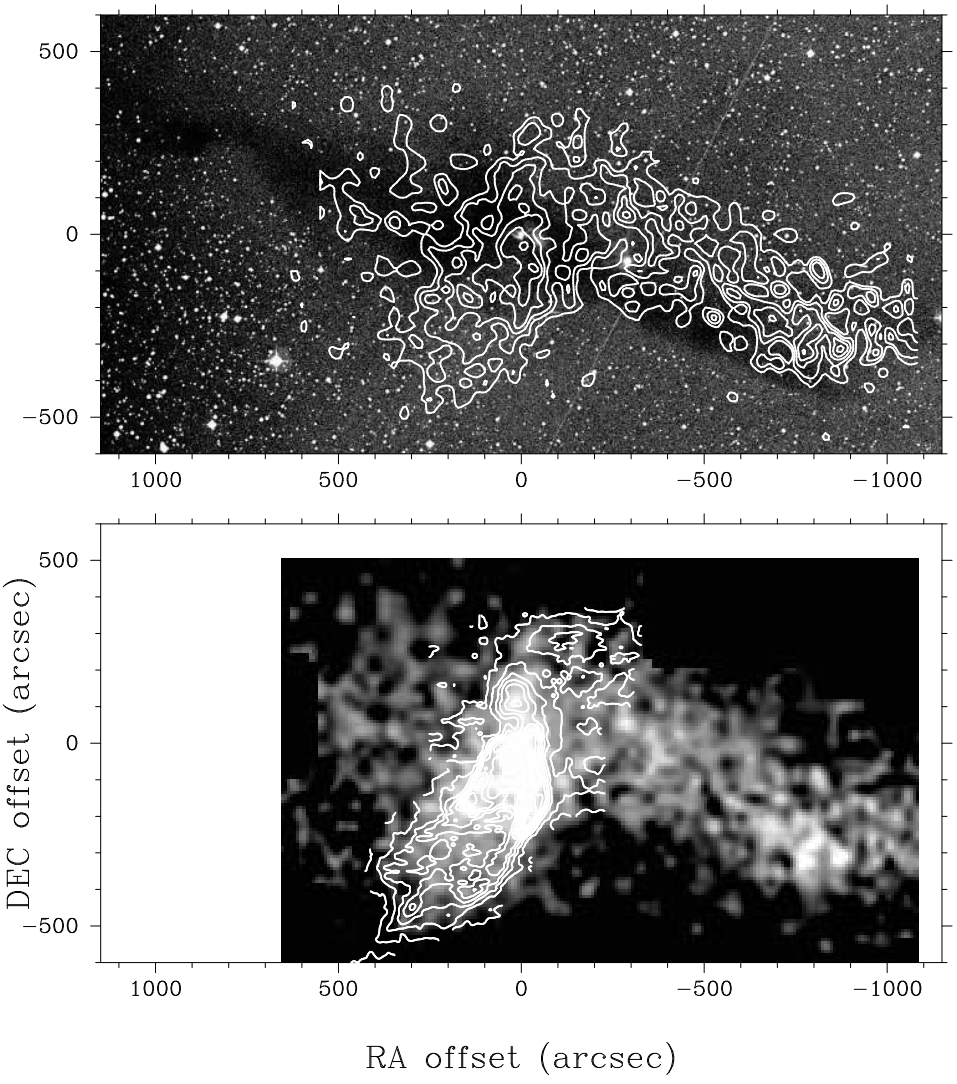

Figure 6. The upper image shows contours of the integrated intensity $\int_{-5}^{5} T_{\rm R}^{*} {\rm d}v$ of the ^{12}CO $J = 1 \rightarrow 0$ map from the FCRAO 14-m telescope overlaid on the red POSS plate of the region. The contours are at $(1 + 0.2n)$ K km s^{-1}. The lower image shows a grey-scale of the CO $J = 1 \rightarrow 0$ map, with CO $J = 2 \rightarrow 1$ contours overlaid. The contours are at the same levels as in Fig. 2.

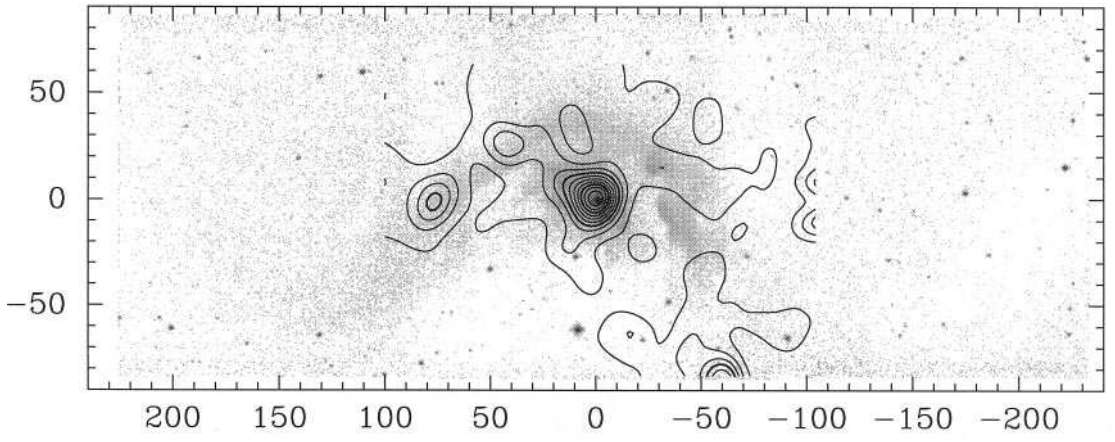

Figure 7. K' band continuum from Hodapp (1994) with a peak of 0.33 Jy, with 450-μm continuum contours overlaid. Offsets are in arcsec from the YSO. The restored 450-μm map has been re-convolved with a 10-arcsec Gaussian so that the smallest features have this beamsize. The 10 contours are at $0.02 + 0.02n$ Jy arcsec^{-2} for $n = 0, 1, \ldots, 9$.

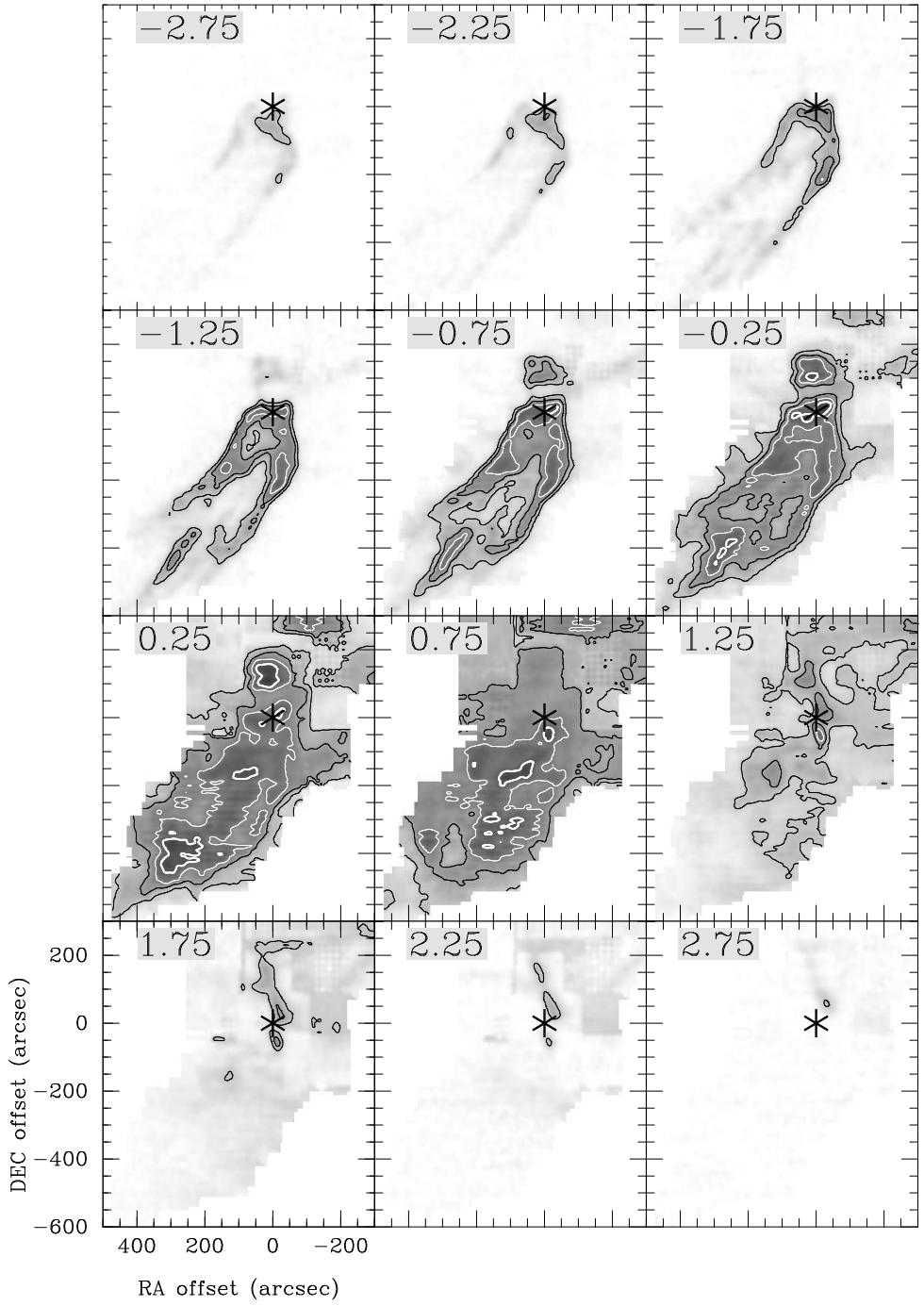

Figure 8. CO $J = 2 \rightarrow 1$ channel maps of the L 43 outflow. Each map shows the integrated intensity $\int T_R^* dv$ in a 0.5 km s^{-1}channel. The centre velocity (V_{LSR}) is shown to the top left of each map. The maps have been convolved to a resolution of ~25 arcsec. Contours on each map are at $(1.5 + 0.5n)$K km s^{-1}for $n = 0, 1, 2, 3, 4$.

overlapping emission originating from their two lobes [see Cabrit & Bertout (1986) for a full discussion].

5.3 Global cloud structure

It is evident from the large scale structure of the L 43 molecular cloud in the $J = 1 \rightarrow 0$ line (Fig. 6), that, despite the ubiquity of CO, the outflow (as seen in CO $J = 2 \rightarrow 1$) is still visible in the lower-excitation line. It is also clear that the outflow fills a large fraction of the total cloud volume. The boundary between regions that have been affected, and those that have not (as seen from the higher excitation $J = 2 \rightarrow 1$ map), is very clear, even in the integrated intensity of the $J = 1 \rightarrow 0$ map. The enhanced integrated intensity in the outflowing regions is almost entirely caused by an increase in the linewidths, rather than an increase in the peak temperature. It is these regions of enhanced linewidth that we have referred to as disturbed, with typical undisturbed linewidths being $\lesssim$0.5 km s^{-1}. [We note that a similar correspondence between FCRAO $J = 1 \rightarrow 0$ and JCMT $J = 2 \rightarrow 1$ maps can be seen in the RNO 43, L 1262 and L 588 outflows (Bence et al., in preparation).] Rapid mapping is

unable to locate regions of high-velocity emission directly, since this emission tends to be at low levels. Nevertheless the integrated intensity clearly follows the outflow, and the peaks in integrated intensity correlate well with the high-velocity regions found in the $J = 2 \rightarrow 1$ map: low-frequency mapping may thus prove useful as a way of finding regions with broad line-wings. Of course, whilst outflow activity appears to imply high integrated intensities, the reverse is not necessarily true.

5.4 Physical parameters of the southern lobe

The CO to the south of RNO 91 extends about 0.3 pc beyond the obvious optical extinction on the POSS plates. This suggests that dark regions on optical plates may be poor indicators of molecular material and we thus emphasise the importance of large-scale mapping of outflows – not concentrating on the dense core regions demarcated by extinction on optical plates.

Assuming that the CO is optically thin in the southern lobe, and that the excitation temperature is 10 K, we find a total mass of 0.07 $M_\odot$ lying beyond the obvious edge of the cloud. This should be compared with the mass of the dense core surrounding RNO 91, which Myers & Benson (1983) measure to be 2 $M_\odot$ using ammonia observations. It seems likely, however, that the core has been significantly disrupted by the outflow activity given the reflection nebulosity to the south of the source, and thus some of the ejected mass has been hidden, presumably by UV dissociation. This is entirely plausible since, if the flow pattern of the southern lobe is propagating away from the cloud at about 2 km s^{-1}(see Section 6), then CO has been exposed to background UV radiation for about 50 000 yr. This is much longer than the lifetime for unshielded CO in a $G = G_0$ UV field, which is a few hundred years (Van Dishoeck & Black 1988), and so it is perhaps surprising that *any* CO is observed. Presumably some of the CO has been shielded from the UV field by dust. This is supported by the IRAS 100-μm image which shows emission extended in the direction of the southern CO lobe.

Given that significant UV dissociation appears to have taken place, estimates for the momentum and energy of the southern lobe are subject to serious errors. Lower limits can be obtained, however, and are found to be 0.03 $M_\odot$ km $s^{-1}$for the blueshifted momentum, 0.01 $M_\odot$ km $s^{-1}$for the redshifted momentum and a total energy of 8×10^{28} J [for comparison, the NGC 2264G outflow has a mass of 0.8 $M_\odot$, a momentum of 10 $M_\odot$ km s^{-1}, and an energy of 1.6×10^{31} J (Lada & Fich 1996)].

5.5 Poor collimation

Although there appears to be a relatively narrow jet-like feature at PA +13°, the outflow in L 43 is generally poorly collimated with the extreme edges subtending an angle of several tens of degrees at the YSO. A number of other sources, for example L 1551 IRS 5 (Snell et al. 1980), show similar low collimation. In at least some sources, however, we know that molecular material is swept up and accelerated via an interaction with a highly collimated jet. If we believe that *all* molecular outflows are driven by collimated jets (at least at some stages of their evolution), then we must explain the observed broadening in L 43. One way is to invoke a wandering of the jet direction; another is to posit that old outflows are driven by a wide-angled wind catching up with an existing shell. Alternatively, the observed limb-brightened shell may be maintained by the thermal pressure of a hot low-emissivity medium interior to the shell. A final possibility is that the shell is coasting in a 'snowplough' phase (Castor, McCray & Weaver 1975; Lada 1985; Margulis, Lada & Snell 1988).

As pointed out to us by the referee, outflows have considerable momentum, and even if the driving force is instantaneously turned off, will continue to coast in a momentum-conserving fashion, with the deceleration determined by the rate at which mass accumulates in the shell. For a coasting spherical shell propagating in a uniform external medium, the shell radius increases as $R_s \propto t^{1/4}$, $v_s \propto t^{-3/4}$; for a cylindrical shell, such as L43 more closely resembles, these relations become instead $R_s \propto t^{1/3}$, $v_s \propto t^{-2/3}$. This snowplough phase continues until the ram pressure of the external medium on the shell is comparable to the thermal pressure in the external medium, or equivalently, until the shell velocity equals the sound speed. After this the shell should disperse into the ambient medium.

In the case of the L43 outflow, we show in Section 6 that the structure is compatible with a thin expanding shell with mean expansion velocity of about 1 km s^{-1}. The sound speed in the external medium on the other hand is at least 0.4 km s^{-1}, and higher than this if the temperature is greater than 10 K or if there is any significant magnetic field (in which case the Alfvén speed is the appropriate measure of random velocity dispersion). This uncertainty in the external sound speed makes it very difficult to determine whether or not a continuing energy supply is *required* by the observations. If the external sound speed is only 0.4 km $s^{-1}$and the shell is indeed coasting, then the scalings above suggest that it will continue to grow only until it is approximately 60 per cent larger than its current size, but that it will not reach this size until it is four times its current age. In this case there would be no need at all to invoke a continuing energy supply. If, on the other hand, the external temperature is more like the 100 K typical of atomic clouds and these low visual extinctions, then we are either fortuitously observing the L43 shell right at the end of its life, or it is in fact driven. On the evidence available to us we can't distinguish between these cases, so we now discuss the remaining possibilities in turn.

5.5.1 Wandering jet direction

One possible way to broaden an outflow while retaining a jet model, is to invoke a wandering of the jet direction. High-resolution observations of RNO 43, for example, reveal an intrinsic collimation higher than had previously been observed in that source [see Bence et al. (1996)]. Could it be that L 43 in fact consists of many separate bowshocks, each driven by a current bowshock interaction, but unresolved by the angular resolution available?

This seems unlikely for two reasons. First, even in cases where individual bowshocks are not resolved, lower spatial resolution observations still show localised regions of high velocity material.[1] Except close to the YSO, no such high velocity emission is seen in L 43. Furthermore, the L 43 outflow is relatively nearby (at a distance of 160 pc), and so it is unlikely that individual bowshocks are unresolved as a result of distance effects (we can easily resolve bowshocks even in more distant sources such as RNO 43).

Secondly, many of the linear features visible in the integrated intensity map (Fig. 1) and in the channel maps (Fig. 8) do not align with the YSO, and so are unlikely to have resulted from the passage of a jet emerging from the YSO. These features have large angular scales and it is difficult to imagine a mechanism by which such

[1] An example of this is provided by early observations of RNO 43 with a beamsize of 45 arcsec (Cabrit, Goldsmith & Snell 1988). These showed high velocities associated with the northern bowshocks, even though the individual bowshocks were not resolved.

coherence can be maintained by many, essentially decoupled, bowshocks.

5.5.2 *Wide-angled wind*

The morphology of the southern lobe in L 43 suggests that the outflow consists of a slowly expanding shell of molecular material surrounding a low emissivity cavity (a kinematic model is presented in Section 6). One possibility is that this shell is maintained by the ram pressure of a wide-angled wind from the central star. This is certainly plausible if the degree of collimation of the mass-loss from a YSO decreases with age (a lower collimation may be consistent, since the central source, RNO 91, is apparently in a late stage of evolution). It certainly seems to be the case that the best collimated outflows are associated with young, Class 0, YSOs, and further that the accretion rate from the disc onto the YSO may decrease substantially with age (Bontemps et al. 1996). Further, in L 1551 IRS5, there is evidence that the collimation of the driving wind varies in time (Davis et al. 1995).

A wide-angled wind model has been discussed by Shu et al. (1991). The posited wind is, at all positions, directed radially away from the YSO, forming a self-similar shell of swept-up material. One of the principle objections to this model is that it fails to reproduce observed spectral-line shapes (Masson & Chernin 1992). The model predicts that those parts of the shell furthest away from the YSO must have the highest velocities and so will have swept up most material, i.e. a large fraction of the total outflowing material must be moving at high velocity. The average spectrum in L 43, on the other hand (Fig. 5), shows that there is a rapid fall-off of mass with velocity. Furthermore, the wide-angled wind model predicts that the highest velocities will be observed furthest from the YSO, and this is not observed in L 43.

On the other hand, Li & Shu (1996) have recently shown that if the wide-angle wind originates in a oblate toroidal cloud core, then the observed variations of outflow mass with velocity can in fact be modelled quite well. This model has recently been successfully applied to the HH 111 outflow and jet by Nagar et al. (1997). It therefore does not appear to be possible to rule out wide-angle winds as a driving force on grounds of the mass-velocity distribution alone.

However, although it is thus not *required* by the observations, it is equally possible that at some time in the past a powerful jet from the YSO cleared molecular material away from the molecular cloud to create a shell. The now evolved YSO may then be currently driving a much weaker, poorly collimated wind which, unopposed by a significant mass of ambient material, may be able to *maintain* the shell. This is similar to the situation observed in planetary nebulae. Like young stellar objects, stars on the asymptotic giant branch undergo a phase of mass loss. In the standard models of these planetary nebulae (Kwok, Purton & Fitzgerald 1978; Balick 1987) a low-velocity stellar wind is generated during this stage of evolution. As the star approaches the end of the asymptotic giant branch, the wind suddenly becomes much faster and this new wind catches up with its precursor, and in doing so forms an expanding shocked shell. Just as in the interpretation of the L 43 outflow given above, environmental effects are thought to break the expected symmetry to produce the wide variety of morphologies observed (Balick, Preston & Icke 1987; Dwarkadas, Chevalier & Blondin 1996), some of which are remarkably similar to L 43.

5.5.3 *Pressure-driven bubble*

A final possibility is that the observed slowly expanding shell has been produced by the thermal pressure of a hot medium in the interior of the shell. This 'energy driven' outflow model has been discussed by Canto (1980) and Kwok & Volk (1985) but has previously been discounted, especially for those outflows that are highly collimated. L 43, on the other hand, is not highly collimated, and the argument that a pressure-driven shell produces too much motion transverse to the outflow axis does not apply to L 43, since the velocities are low and the velocity structure suggests that there is in fact a significant amount of transverse motion.

We have thus identified three mechanisms which could be responsible for the observed structure seen in L 43, namely a wide-angled wind, a pressure-driven bubble, or a pure coasting expansion. An expanding shell model thus looks promising and in Section 6 we investigate it further by developing a kinematic model.

6 A KINEMATIC MODEL

A schematic picture of an expanding shell is shown in Fig. 9. Assuming that there is no variation of velocity structure along the outflow axis, it can be seen that the emission seen by the observer will be symmetric about $v_z \sin\theta$, where θ is the angle of inclination of the outflow axis to the sky, and v_z is a characteristic velocity along the outflow axis. We shall now define the nomenclature used to describe an expanding, axisymmetric, shell.

We shall assume that at any point the radial component of the velocity has a Gaussian profile of mean μ_{v_r} and variance $\sigma^2_{v_r}$. Then

$$f_1(v_r) = \frac{1}{\sigma_{v_r}\sqrt{2\pi}} \exp\left[-\frac{1}{2}\left(\frac{v_r - \mu_{v_r}}{\sigma_{v_r}}\right)^2\right], \tag{2}$$

where $f(v_r)$ is a probability density function.

Similarly, the longitudinal component of the velocity has a Gaussian profile of mean μ_{v_z} and variance $\sigma^2_{v_z}$, so that

$$f_2(v_z) = \frac{1}{\sigma_{v_z}\sqrt{2\pi}} \exp\left[-\frac{1}{2}\left(\frac{v_z - \mu_{v_z}}{\sigma_{v_z}}\right)^2\right]. \tag{3}$$

Combining these distributions we obtain a two-dimensional Gaussian distribution:

$$f_3(v_r, v_z) = \frac{1}{\sigma_{v_r}\sigma_{v_z}2\pi} \exp\left[-\frac{1}{2}\left\{\left(\frac{v_r - \mu_{v_r}}{\sigma_{v_r}}\right)^2 + \left(\frac{v_z - \mu_{v_z}}{\sigma_{v_z}}\right)^2\right\}\right]. \tag{4}$$

Now, taking the projection of this onto our line of sight, we get a new one-dimensional Gaussian distribution,

$$f_4(v_p) \propto \frac{1}{\sigma_{v_p}\sqrt{2\pi}} \exp\left[-\frac{1}{2}\left(\frac{v_p - \mu_{v_p}}{\sigma_{v_p}}\right)^2\right], \tag{5}$$

where

$$\mu_{v_p} = \mu_{v_r}\cos\theta\cos\phi + \mu_{v_z}\sin\theta, \tag{6}$$

and

$$\sigma^2_{v_p} = \sigma^2_{v_r}\cos^2\theta\cos^2\phi + \sigma^2_{v_z}\sin^2\theta, \tag{7}$$

and ϕ is the polar angle in cylindrical polar coordinates.

In fact, the mean and variance of this distribution may be functions of radius r, and specifically, it is reasonable to assume that the velocity of the outer part of the shell is zero, i.e. $v_{r=b} = 0$. In order to calculate the emission at a particular radius we must also weight the intensity by the volume element in cylindrical polar coordinates, i.e. by $r\Delta r\Delta\phi\Delta z$.

Finally, for direct comparison with observations a Gaussian component must be added at the cloud $V_{\rm LSR}$.

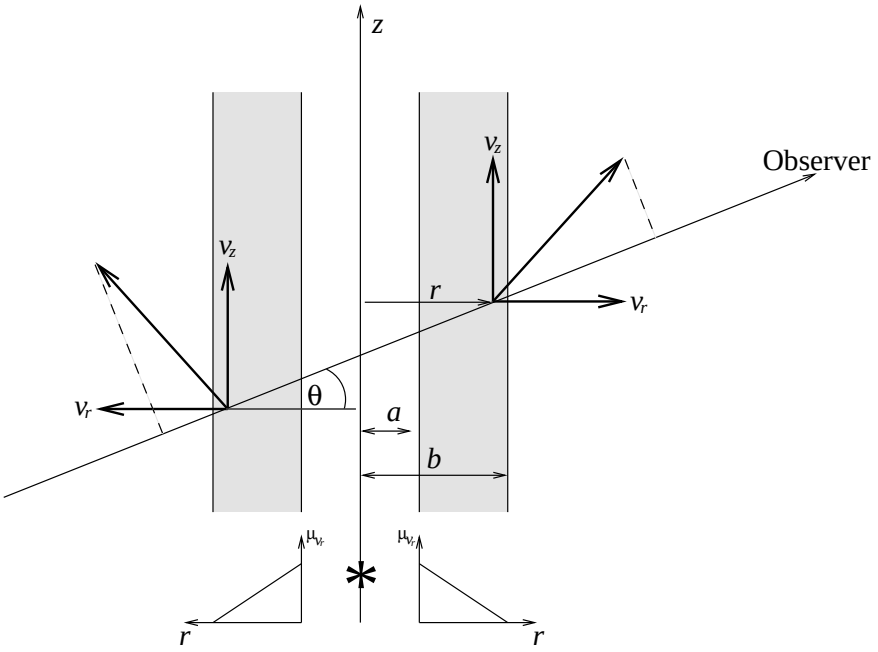

Figure 9. Model of an expanding shell. The shell is axisymmetric and inclined at an angle θ to the plane of the sky. Two components contribute to the line-of-sight velocity; motion along and transverse to the outflow axis. The parameters a and b give the inner and outer dimensions of the shell and the viewing angle by the observer is θ.

The simplest comparison which can be made between the observations and the kinematic model is via position–velocity diagrams perpendicular to the outflow axis. Referring back to Fig. 1, the first thing to notice is that the limb-brightened edges of the emission are narrow (< 40 arcsec, while the effective beamsize, after the convolution, is 25 arcsec) and almost linear along the whole length. The region between the two edges is relatively devoid of emission, and, as can be seen in the channel maps, this is particularly so at high velocities. In general the emission is weaker further from the YSO. Note that the shell is not quite symmetric about a line at 35° to the vertical which passes through the YSO.

The features discussed above can all be seen in the position–velocity cuts, perpendicular to the outflow axis, shown in Fig. 10. Plot (a) shows the position–velocity structure in the innermost region of the outflow, i.e. close to the YSO. The edges of the shell can be seen, together with a component in the centre of the bubble. Plot (b) is most representative of the structure inside the bubble, showing that the emission is much lower there. It also shows that, for any particular velocity, the peak of the emission always occurs at much the same place. It is also evident from this plot that the peak of the line is blueshifted by about 0.5 km s^{-1}, with respect to the ambient gas, within the 'bubble region'. This is the plot with which detailed comparison with the kinematic model is most appropriate. In plot (c) the weak southern jet can be seen. The contour levels in all the plots are the same, and it should be noticed that plot (a) is very similar to plot (b) if the lowest contour is ignored. Thus, only plot (c) is significantly different.

Plot (d) of Fig. 10 shows a synthetic position–velocity diagram made using the kinematic model previously presented; this plot should be compared to the second plot, which is taken at the midpoint of the bubble. In the model used to produce this figure the radial velocity profile has $\mu_{v_r} = 2.0$ km s^{-1} at the inner edge and $\sigma_{v_r} = 1.0$ km s^{-1}, the longitudinal velocity profile has $\mu_{v_z} = -2$ km s^{-1} and $\sigma_{v_z} = 1.0$ km s^{-1}, the shell has $a = 60$ arcsec, $b = 100$ arcsec, and the angle of inclination to the observer is 45°. No account has been taken of any variation along the axis of the outflow.

It can be seen that the kinematic model produces all the essential features of the observed position–velocity diagrams. The Gaussian central component has been matched to the observed central component outside the bubble. The width and separation of the two blueshifted cusps is determined by the dimensionless parameter a/b, together with the convolution. The dip in the centre of the bubble is caused by the geometrical effect of looking through less shell width in the centre – its magnitude is also determined by the ratio a/b. Thus the structure results predominantly from geometrical limb-brightening. The velocity structure, of course, depends on the velocity Gaussians assumed in the model. The emission from the shell is symmetric about the projected mean longitudinal velocity, i.e. about $\mu_{v_z} \sin\theta$ but the redshifted side is masked by the Gaussian central component, and this introduces the asymmetry. This effect is also responsible for the systematic blueshift of the peak of the line within the bubble region. Finally the dispersion in the velocity in the cusps is caused by the dispersion of the velocity from its maximum on the inner edge of the shell, to zero on the outer edge; this means that the intrinsic radial dispersion σ_{v_r} can take an arbitrary low value (it has been chosen to be the same as σ_{v_z}). The dispersion in the centre is dominated by the longitudinal dispersion σ_{v_z}, and by that in the ambient cloud.

7 COMPARISON WITH OTHER SOURCES

A number of well-studied outflows do not fit into the current picture of molecular jets. The optical emission in the archetypical L1551-IRS5 outflow, for example, shows relatively poor collimation on large scales, and also a 'bay' similar to that seen in L 43. Davis et al. (1995) suggest that the driving jet in this source undergoes episodic changes in collimation, such that the inner 'jet' is caused by a well-collimated current phase, but that the extended emission is caused

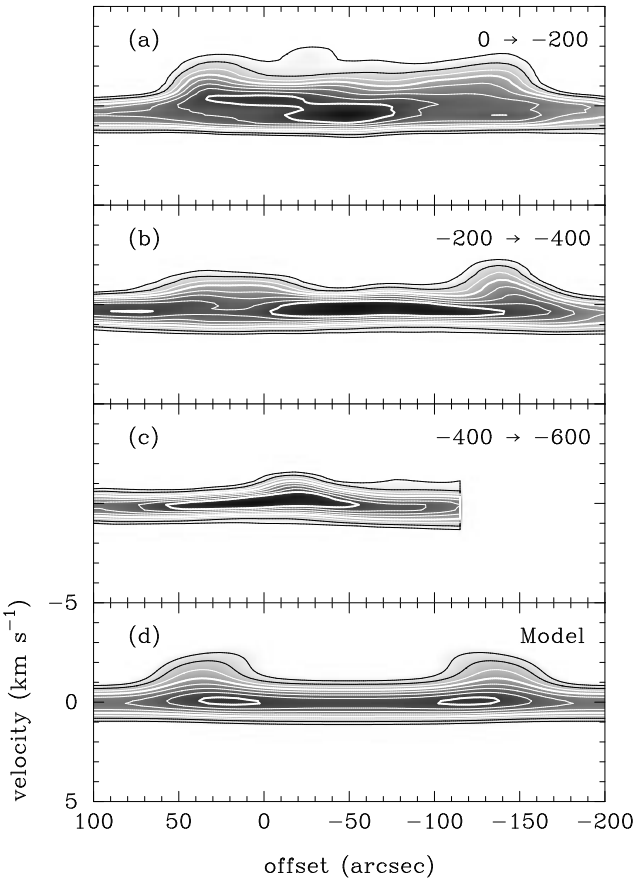

Figure 10. Position–velocity diagrams transverse to the principal axis of the L 43 outflow. Plot (a) is averaged from $0 \rightarrow -200$ arcsec from the YSO, plot (b) from $-200 \rightarrow -400$ arcsec and plot (c) from $-400 \rightarrow -600$ arcsec. The limits of these cuts are shown in Fig. 1. Plot (d) is a synthetic plot produced using the kinematic model presented in the text.

by a previous episode in which the jet was poorly collimated. They further conclude that a steady two component (wide-angled wind & jet) model cannot explain the observations. In their model the cometary reflection nebula is also caused by a previous wide-angled wind phase. The collimation of the CO is also poor (Moriarty-Schieven et al. 1987). These authors suggest that the outflow consists of a narrow, expanding shell, similar to that seen in L 43.

Another example of a poorly collimated outflow is NGC 2261 (Canto et al. 1981). This too shows a parabolic cometary nebula and poorly collimated CO emission. The authors conclude that the bubble which has been inflated, is re-collimated towards its terminus, such that it excites further optical emission. The 450 μm continuum image of the centre of the L 43 dark cloud bears a striking resemblance to the 1.3-cm continuum image of the S 106 region (Felli et al. 1984), despite the different emission mechanisms. S 106 hosts a high-mass protostar, and it seems that similar evacuation of a cavity may be occurring in both this and in L 43. Further examples of poorly collimated optical flows are Cep A (Corcoran, Ray & Mundt 1993), V 380 Ori (Corcoran & Ray 1995) and HH 7–11 (Davis et al. 1995).

The obvious next question is whether these two types of molecular outflow – collimated and poorly collimated – represent two distinct classes of outflow characterised by fundamentally different physical processes, or whether they represent different evolutionary phases of one phenomenon. A limited sample of outflows is insufficient to be able to successfully answer this question, and a much larger set of maps of *overall* outflow structure is required.

8 CONCLUSIONS

We have shown that the L 43 outflow covers a much larger area of sky than had previously been thought, and extends beyond the obvious boundaries of its parent cloud, as defined by high optical extinction. The breadth of the outflow does not appear to be explained by a precessing narrow jet. The available data do not allow us to rule out pure coasting expansion, although it is likely that this would require us to be observing the source close to the time at which the shell disperses into the surrounding ISM. If the shell is currently being driven, then one possibility is that the expanding shell structure is maintained by an intrinsically poorly collimated wind similar to the situation observed in L 1551 IRS5, where a neutral H I wind has been detected at velocities up to 260 km s^{-1} (Giovanardi et al. 1992). A similar search for H I in L 43 should prove interesting. Alternatively the shell may be produced by the thermal pressure of a hot medium interior to the bubble.

The outflow has evacuated a cavity to the south of the driving source, and this can be seen in enhanced infrared and submillimetre continuum emission. Thus, it seems that the outflow is in the process of dispersing its parent cloud, a process which will eventually expose the star.

Finally, we have shown that rapid mapping of the outflow in the CO $J = 1 \rightarrow 0$ line shows many of the features seen in the more detailed, time-consuming, $J = 2 \rightarrow 1$ maps. The total time spent observing the FCRAO map was about 20 per cent of the time spent observing the JCMT map, and the map covers about twice the area. Furthermore, the weather was particularly poor for the FCRAO observations and the observing airmass much higher than for the JCMT observations. We thus estimate that low-frequency mapping with a large beam and an array receiver should be able to identify the total extent of molecular outflows many times faster than single beam high frequency observations. Using this technique on a larger sample of outflows should significantly reduce the total time required to observe entire outflows, making statistical comparisons possible.

ACKNOWLEDGMENTS

The JCMT and the UKIRT are operated by the Royal Observatories, on behalf of the Particle Physics and Astronomy Research Council of the United Kingdom, the Netherlands Organisation for Pure Research and the National Research Council of Canada. The Five College Radio Astronomy Observatory is operated with the support of the National Science Foundation under grant AST94-20159 and with the permission of the Metropolitan District Commission of Massachusetts. SJB thanks the PPARC and the Mullard Fund. MCW thanks the German Academic Exchange Service and the Isaac Newton Studentship Fund. We thank C. J. Lada for helpful comments.

REFERENCES

André P., Montmerle T., 1994, ApJ, 420, 837
Balick B., 1987, AJ, 94, 671
Balick B., Preston H. L., Icke V., 1987, AJ, 94, 1641
Bence S. J., Richer J. S., Padman R., 1996, MNRAS, 279, 866
Bontemps S., André P., Terebey S., Cabrit S., 1996, A&A, 311, 858
Cabrit S., Bertout C., 1986, ApJ, 307, 313

Cabrit S., Goldsmith P. F., Snell R. L., 1988, ApJ, 334, 196
Canto J., 1980, A&A, 86, 327
Canto J., Rodriguez L. F., Barral J. F., Carral P., 1981, ApJ, 244, 102
Castor T., McCray R. M., Weaver R., 1975, ApJ, 200, L107
Chernin L. M., Masson C. R., 1991, ApJ, 383, L93
Cohen M., 1980, A&A, 85, 29
Corcoran D., Ray T. P., 1995, A&A, 301, 729
Corcoran D., Ray T. P., Mundt R., 1993, A&A, 279, 206
Davis C. J., Mundt R., Eisloffel J., Ray T. P., 1995, AJ, 110, 766
Dent W. R. F., Matthews H. E., Walther D. M., 1995, MNRAS, 277, 193
Dwarkadas V. V., Chevalier R. A., Blondin J. M., 1996, ApJ, 457, 773
Elmegreen D. M., Elmegreen B. G., 1979, AJ, 84, 615
Felli M., Massi M., Staude H. J., Reddmann T., Eiroa C., Hefele H., Neckel T., Panagia N., 1984, AA, 135, 261
Fukui Y., Iwata T., Mizuno A., Bally J., Lane A. P., 1993, Protostars & Planets III. Univ. Arizona, Tucson, p. 603
Giovanardi C., Lizano S., Natta A., Evans N. J., Heiles C., 1992, ApJ, 397, 214
Herbst W., Warner J., 1981, AJ, 86, 885
Hodapp K.-W., 1994, ApJS, 94, 615
Kwok S., Purton C. R., Fitzgerald P. M., 1978, ApJ, 219, L125
Kwok S., Volk K., 1985, ApJ, 299, 191
Lada C. J., 1985, ARA&A, 23, 267
Lada C. J., Fich M., 1996, ApJ, 459, 638
Levreault R. M., 1988, ApJ, 330, 897
Li Z. Y., Shu F. H., 1996, ApJ, 468, 261
Margulis M., Lada C. J., Snell R. L., 1988, ApJ, 333, 316
Masson C. R., Chernin L. M., 1992, ApJ, 387, L47
Mathieu R. D., Benson P. J., Fuller G. A., Myers P. C., Schild R. E., 1988, ApJ, 330, 385
Moriarty-Schieven G. H., Snell R. L., 1988, ApJ, 332, 364
Moriarty-Schieven G. H., Snell R. L., Strom S. E., Schloerb F. P., Strom K. M., Grasdalen G. L., 1987, ApJ, 319, 742
Myers P. C., Benson P. J., 1983, ApJ, 266, 309
Myers P. C., Heyer M. L., Snell R., Goldsmith P. F., 1988, ApJ, 324, 907
Nagar N. M., Vogel S. N., Stone J. M., Ostriker E. C., 1997, ApJ, 482
Parker N. D., Padman R., Scott P. F., 1991, MNRAS, 252, 442
Parker N. D., Padman R., Scott P. F., Hills R. E., 1988, MNRAS, 234, 67P
Raga A. C., Cantó J., Calvet N., Rodríguez L. F., Torrelles J. M., 1993, AA, 276, 539
Richer J., 1992, MNRAS, 254, 165
Richer J. S., Hills R. E., Padman R., 1992, MNRAS, 254, 525
Scarrott S. M., Draper P. W., Tadhunter C. N., 1993, MNRAS, 262, 306
Schild R., Weir N., Mathieu R. D., 1989, AJ, 97, 1110
Shu F., Roden A., Lada C., Lizano S., 1991, ApJ, 370, L31
Snell R. L., Loren R. B., Plambeck R. L., 1980, ApJ, 239, L17
Staude H. J., Elsasser H., 1993, ARA&A, 5, 165
Stevens J. A., Robson E. I., 1994, MNRAS, 270, L75
Terebey S., Chandler C. J., André P., 1993, ApJ, 414, 759
van Dishoeck E., Black J., 1988, ApJ, 334, 771
Whitney B. A., Hartmann L., 1993, ApJ, 402, 605
Wu Y., Huang M., He J., 1996, A&AS, 115, 283

This paper has been typeset from a TEX/LATEX file prepared by the author.